




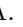









# Spin and lattice dynamics at the spin-reorientation transitions in the rare-earth orthoferrite $\text{Sm}_{0.55}\text{Tb}_{0.45}\text{FeO}_3$

R. M. Dubrovin <sup>1,\*</sup> A. I. Brulev <sup>1,2</sup> N. R. Vovk <sup>3</sup> I. A. Eliseyev <sup>1</sup> N. N. Novikova <sup>4</sup>  
V. A. Chernyshev <sup>5</sup> A. N. Smirnov <sup>1</sup> V. Yu. Davydov <sup>1</sup> Anhua Wu <sup>6</sup>  
Liangbi Su <sup>6</sup> R. V. Mikhaylovskiy <sup>3</sup> A. M. Kalashnikova <sup>1</sup> and R. V. Pisarev <sup>1</sup>

<sup>1</sup>*Ioffe Institute, Russian Academy of Sciences, 194021 St. Petersburg, Russia*

<sup>2</sup>*University of Nizhny Novgorod, 603022 Nizhny Novgorod, Russia*

<sup>3</sup>*Department of Physics, Lancaster University, Bailrigg, Lancaster LA1 4YW, United Kingdom*

<sup>4</sup>*Institute of Spectroscopy, Russian Academy of Sciences, 108840 Moscow, Troitsk, Russia*

<sup>5</sup>*Department of Basic and Applied Physics, Ural Federal University, 620002 Yekaterinburg, Russia*

<sup>6</sup>*Shanghai Institute of Ceramics, Chinese Academy of Sciences, 201899 Shanghai, China*

(Dated: October 3, 2025)

Linear and non-linear couplings of magnetic and lattice excitations are at the heart of many fascinating magnetophononic phenomena observed in rare-earth orthoferrites, the distinctive feature of which is the tendency to spin reorientation transitions. Here we report the results of the experimental study of the spin and lattice dynamics in the Brillouin zone center of the rare-earth orthoferrite  $\text{Sm}_{0.55}\text{Tb}_{0.45}\text{FeO}_3$  by using polarized infrared reflectivity and Raman scattering spectroscopic techniques. The obtained results were supported by the first-principles calculations, which allowed us to reliably identify the parameters of most infrared- and Raman-active phonons. We reveal the spin reorientation transitions  $\Gamma_4(G_a F_c) \xleftrightarrow{T_1} \Gamma_{24}(G_{ac} F_{ac}) \xleftrightarrow{T_2} \Gamma_2(G_a F_c)$  at  $T_1 \simeq 220$  K and  $T_2 \simeq 130$  K and carefully studied the following evolution of Raman scattering on magnetic excitations at these transitions. Notably, the intermediate magnetic structure  $\Gamma_{24}$  displays an exceptionally broad temperature range  $\Delta T = T_1 - T_2 \simeq 90$  K in mixed  $\text{Sm}_{0.55}\text{Tb}_{0.45}\text{FeO}_3$  crystal compared to pure rare-earth orthoferrites. We attribute this broadening of the intermediate phase to the modification of the magnetocrystalline anisotropy as a result of the inhomogeneous magnetic structure caused by the random distribution of rare-earth  $\text{Sm}^{3+}$  and  $\text{Tb}^{3+}$  ions. We found no change in the parameters of Raman-active  $B_{1g}$  phonons or the appearance of new phonons induced by spin reorientation transitions which have been reported for  $\text{SmFeO}_3$ . We assume that our results provide a solid basis for experimental and theoretical research within the modern area of magnetophononic phenomena in rare-earth orthoferrites.

## I. INTRODUCTION

Orthoferrites  $\text{RFeO}_3$ , where R stands for a rare-earth cation, have been known for over 60 years and are at the forefront of modern magnetism research throughout that time [1]. They host an astonishing diversity of physical phenomena such as a weak ferromagnetism due to the Dzyaloshinskii-Moriya interaction [2, 3], magnetoelectricity [4–6], multiferroicity [7], electromagnons [8, 9], altermagnetism [10–13], and many others [14]. Orthoferrites hold a particular place as a platform for experimental research in the fields of ultrafast magnetism [15–18], nonlinear phononics [19], magnonics [20–23] and magnetophononics [24, 25]. One of the unique magnetic properties of the rare-earth orthoferrites is their tendency to change one of three symmetry allowed magnetic structures for the iron subsystem labeled by  $\Gamma_1$ ,  $\Gamma_2$ , and  $\Gamma_4$  as a result of spin reorientation transitions under the magnetic interaction between iron  $\text{Fe}^{3+}$  and rare-earth  $\text{R}^{3+}$  cations [1]. The most common spin reorientation transition in orthoferrites is between  $\Gamma_2$  and  $\Gamma_4$  magnetic structures through the intermediate state  $\Gamma_{24}$  [1, 14, 26].

Many papers focus on the study of magnetic [27–31] and lattice [32, 33] dynamics evolution during spin reorientation transition in orthoferrites in order to reveal new effective mechanisms of interaction between iron and rare-earth cations. In this paper, we report results of the experimental study on the lattice and magnetic dynamics in the Brillouin zone center of a rare-earth orthoferrite  $\text{Sm}_{0.55}\text{Tb}_{0.45}\text{FeO}_3$  single crystal employing polarized Raman scattering and infrared reflectivity spectroscopic techniques. The obtained experimental results were supported by the corresponding first-principles lattice dynamics calculations. Furthermore, we explored the Raman scattering spectra of magnon modes for all main polarization configurations in magnetic structures  $\Gamma_2$  and  $\Gamma_4$  and revealed the temperature evolution of these modes in the range of spin reorientation transitions. The interest in this mixed compound arises due to the fact that pure  $\text{SmFeO}_3$  and  $\text{TbFeO}_3$  crystals have a spin-reorientation transition  $\Gamma_4 \leftrightarrow \Gamma_{24} \leftrightarrow \Gamma_2$  between the most common magnetic structures for orthoferrites at very different temperatures, namely above 300 K and below 10 K, respectively [1, 34]. As a consequence, the spin-reorientation transition in mixed orthoferrite  $\text{Sm}_{0.55}\text{Tb}_{0.45}\text{FeO}_3$  may vary in a very broad temperature range, and, in particular, in the vicinity of the room temperature. This property opens potential possibilities for

\* dubrovin@mail.ioffe.ru

developing temperature-controllable magnetic devices.

## II. MATERIALS AND METHODS

### A. Samples

The high-quality single crystals of orthoferrite  $\text{Sm}_{0.55}\text{Tb}_{0.45}\text{FeO}_3$  were grown by the four-mirror floating zone technique, as described in detail in Refs. [35]. The XRD oriented single crystals were cut into samples with a normal of the surface along the three main crystallographic axes and polished to optical surface quality. The samples have a typical thickness of about 1 mm and a surface size of about  $8 \times 8 \text{ mm}^2$ .

### B. Infrared spectroscopy

The infrared reflectivity measurements were carried out at room temperature with near normal incident light (the incident light beam was near at  $13^\circ$  from the normal to the sample surface) using a Bruker IFS 66v/S spectrometer with DTGS ( $50\text{--}450 \text{ cm}^{-1}$ ) and DLaTGS ( $450\text{--}5000 \text{ cm}^{-1}$ ) detectors with a resolution of  $4 \text{ cm}^{-1}$ , a number of scans of 128, and a scanning velocity of  $2.2 \text{ kHz}$ . The linear polarization of light emitted by the global source was set by the THz linear thin film polarizer along the main crystallographic axes of the crystal samples. Absolute values of reflectivity were obtained by normalizing the spectra obtained from the samples by the reference one from the gold mirror.

### C. Raman spectroscopy

The polarized Raman spectra were measured using the Horiba LabRAM HREvo UV-Vis-NIR-Open spectrometer with the 1800 lines/mm grating equipped with a confocal microscope and a liquid nitrogen cooled CCD detector. For excitation, a  $632.8 \text{ nm}$  line of a HeNe laser (Newport N-LHP 928) was used with a power of  $14 \text{ mW}$ . The temperature of the samples in the experiment was varied in the range from  $78$  to  $400 \text{ K}$  using a Linkam thermal stage. Experiments were performed in the backscattering geometry using a Leica PL FLUOTAR  $50\times$  ( $\text{NA} = 0.55$ ) long working-distance objective lens to focus the incident beam into a spot of  $2 \mu\text{m}$  diameter and to collect the scattered light. For measurement at ambient conditions, an Olympus MPLN  $100\times$  objective was used to focus the excitation beam into a spot with a diameter of  $< 1 \mu\text{m}$ . To control the sample temperature in the range from  $78$  to  $400 \text{ K}$ , a Linkam THMS600 nitrogen cryostat was used.

### D. Lattice dynamics calculations

We have supplemented the obtained experimental results by the lattice dynamics calculations performed in the framework of density functional theory (DFT) with B3LYP hybrid functional [36] implemented on CRYSTAL14 package [37]. The quasi-relativistic ECPnMWB pseudo-potentials for  $\text{Tb}^{3+}$  ( $n = 54$ ) and  $\text{Sm}^{3+}$  ( $n = 51$ ) were used to describe the core electrons including  $4f$  shell [38, 39]. To describe the valence electrons of rare-earth ions, the ECPnMWB-I basis sets were used [38, 40]. All electron basis sets have been used to describe ions with a contraction scheme of (842111s)-(6311p)-(411d)-(1f) for Fe, and (6211s)-(411p)-(1d) for O [41]. The putative ferromagnetic spin configuration was used in the calculations. The reciprocal space was sampled by  $8 \times 8 \times 8$   $k$ -point mesh. The parameters that establish the accuracy in evaluating the Coulomb and Hartree-Fock exchange series were set as 8, 8, 8, 8, and 16 [37]. The threshold on the self-consistent field energy was set to  $10^{-9}$  Hartree for the geometry optimization and  $10^{-8}$  Hartree for the frequency calculation. The phonon spectra of  $\text{TbFeO}_3$  and  $\text{SmFeO}_3$  were calculated in harmonic approximation in the center of the Brillouin zone by means of numerical second derivatives of the total energy. The static dielectric tensors, Born effective charges, and phonon intensities were calculated using the CPHF/KS approach [42, 43]. It was shown that the phonon frequencies in rare-earth orthoferrites depend linearly on the ionic radius of the R ion [44]. From this, the phonon frequencies for  $\text{Sm}_{0.55}\text{Tb}_{0.45}\text{FeO}_3$  were estimated using those for  $\text{SmFeO}_3$  and  $\text{TbFeO}_3$  and taking into account the effective ionic radii of the R ion as  $r_R = 0.55 r_{\text{Sm}}(1.079 \text{ \AA}) + 0.45 r_{\text{Tb}}(1.040 \text{ \AA}) \simeq 1.0615 \text{ \AA}$ . The obtained phonon frequencies for  $\text{SmFeO}_3$ ,  $\text{TbFeO}_3$ , and  $\text{Sm}_{0.55}\text{Tb}_{0.45}\text{FeO}_3$  are listed in Table V.

## III. RESULTS AND DISCUSSIONS

### A. Crystal and magnetic structures and phonons

The rare-earth orthoferrite  $\text{Sm}_{0.55}\text{Tb}_{0.45}\text{FeO}_3$  has the orthorhombically distorted perovskite crystal structure with the centrosymmetric space group  $Pbnm$  [No. 62,  $D_{2h}^{16}$ ] and four formula units per unit cell  $Z = 4$  [34]. The  $Pbnm$  is an unconventional setting of the  $Pnma$  space group, which is conventionally used for orthoferrites [1]. The lattice parameters of  $\text{Sm}_{0.55}\text{Tb}_{0.45}\text{FeO}_3$  at room temperature are listed in Table I, in comparison with those of  $\text{SmFeO}_3$  and  $\text{TbFeO}_3$ . The unit cell contains 20 ions occupying the Wyckoff positions  $4c$  for  $\text{Sm}^{3+}$  and  $\text{Tb}^{3+}$ ,  $4b$  for  $\text{Fe}^{3+}$ , and  $4c$  and  $8d$  for  $\text{O}^{2-}$ .

Below the Néel temperature  $T_N(\text{Fe}) \simeq 650 \text{ K}$  the  $\text{Fe}^{3+}$  spins arrangement is a canted antiferromagnetic structure with antiparallel ordering along the  $a$  axis ( $G_a$ ) and a weak ferromagnetic moment along the  $c$  axis ( $F_c$ ) due to the Dzyaloshinskii-Moriya interaction, which corre-

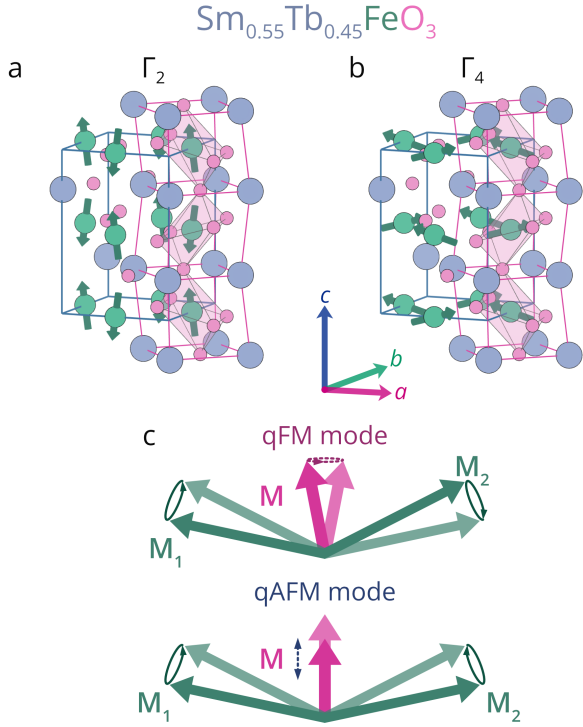


FIG. 1. The crystal and magnetic structures of  $\text{Sm}_{0.55}\text{Tb}_{0.45}\text{FeO}_3$  in the  $Pbnm$  setting in the (a)  $\Gamma_2$  and (b)  $\Gamma_4$  magnetic configurations. (c) The precession of weak ferromagnetic moment  $\mathbf{M} = \mathbf{M}_1 + \mathbf{M}_2$  for quasi-ferromagnetic (qFM) mode and amplitude oscillation of  $\mathbf{M}$  for quasi-antiferromagnetic (qAFM) mode in orthoferrites.

sponds to the  $\Gamma_4(G_aF_c)$  magnetic structure in Bertaut's notation.  $\text{SmFeO}_3$ ,  $\text{Sm}_{0.55}\text{Tb}_{0.45}\text{FeO}_3$  and  $\text{TbFeO}_3$  exhibit one of the most common spin reorientation transitions in orthoferrites in which the  $\text{Fe}^{3+}$  spins are rotated continuously in the  $ac$  plane in the temperature range from  $T_1$  to  $T_2$  ( $T_2 < T_1 < T_N$ ) from the  $\Gamma_4(G_aF_c)$  [Fig. 1(b)] to  $\Gamma_2(G_cF_a)$  [Fig. 1(a)] through the intermediate  $\Gamma_{24}(G_{ac}F_{ac})$  state [34, 46]. The highest spin reorientation transition temperatures  $T_1 \simeq 480$  K and  $T_2 \simeq 450$  K are observed in  $\text{SmFeO}_3$  [32]. Isovalent substitution in  $\text{Sm}_{1-x}\text{R}_x\text{FeO}_3$  reduces the transition temperatures  $T_1$  and  $T_2$  to the required values by varying the concentration of  $\text{R}^{3+}$  ions [14, 34, 35].

The group-theoretical analysis of  $Pbnm$  orthoferrites  $\text{RFeO}_3$  predicts 60 phonons at the center of the Brillouin

TABLE I. Lattice parameters  $a$ ,  $b$ , and  $c$  (in Å), unit cell volume  $V$  (in Å<sup>3</sup>), static  $\epsilon_0$  and high-frequency  $\epsilon_\infty$  anisotropic dielectric permittivities in  $\text{SmFeO}_3$ ,  $\text{TbFeO}_3$ , and  $\text{Sm}_{0.55}\text{Tb}_{0.45}\text{FeO}_3$  obtained from experiments in comparison with our results of DFT calculations.

	$\text{SmFeO}_3$		$\text{TbFeO}_3$		$\text{Sm}_{0.55}\text{Tb}_{0.45}\text{FeO}_3$	
	Exp. <sup>a</sup>	DFT	Exp. <sup>b</sup>	DFT	Exp.	DFT
$a$	5.400	5.475	5.365	5.404	5.395	5.443
$b$	5.584	5.700	5.634	5.684	5.612	5.693
$c$	7.768	7.820	7.623	7.755	7.688	7.791
$V$	234.23	244.04	230.39	238.21	232.77	241.42
$\epsilon_0^a$	—	33.331	21.7	31.886	25.18	32.681
$\epsilon_0^b$	—	30.96	20.5	29.426	23.58	30.270
$\epsilon_0^c$	—	30.182	22.6	31.081	24.86	30.587
$\epsilon_\infty^a$	—	5.215	4.81	5.141	5.4	5.182
$\epsilon_\infty^b$	—	5.237	4.82	5.203	5.39	5.222
$\epsilon_\infty^c$	—	5.094	4.79	5.017	5.36	5.059

<sup>a</sup> Ref. [44].

<sup>b</sup> Ref. [45].

zone [47]:

$$\begin{aligned}
 \Gamma_{\text{total}} = & \underbrace{B_{1u}(z) \oplus B_{2u}(y) \oplus B_{3u}(x)}_{\Gamma_{\text{acoustic}}} \\
 & \oplus \underbrace{7B_{1u}(z) \oplus 9B_{2u}(y) \oplus 9B_{3u}(x)}_{\Gamma_{\text{IR}}} \\
 & \oplus \underbrace{7A_g(x^2, y^2, z^2) \oplus 7B_{1g}(xy) \oplus 5B_{2g}(xz) \oplus 5B_{3g}(yz)}_{\Gamma_{\text{Raman}}} \\
 & \oplus \underbrace{8A_u(xyz)}_{\Gamma_{\text{silent}}},
 \end{aligned} \tag{1}$$

among which there are 3 acoustic, 25 infrared-active, 24 Raman-active, and 8 silent modes. The basis functions are given in parentheses.

## B. Infrared-active phonons

The infrared reflectivity spectra measured for the electric field  $\mathbf{E}$  of radiation polarized along the  $a$ ,  $b$ , and  $c$  axes of  $\text{Sm}_{0.55}\text{Tb}_{0.45}\text{FeO}_3$  at room temperature are shown by the green lines in Figs. 2(a)–2(c), respectively. The reflection bands in the spectra correspond to the  $B_{1u}$ ,  $B_{2u}$ , and  $B_{3u}$  phonons, which are active for specific polarizations according to Eq. (1). These reflectivity spectra were fitted by using the factorized form of the complex dielectric permittivity [48]

$$\epsilon(\omega) = \epsilon_1(\omega) - i\epsilon_2(\omega) = \epsilon_\infty \prod_j \frac{\omega_{j\text{LO}}^2 - \omega^2 + i\gamma_{j\text{LO}}\omega}{\omega_{j\text{TO}}^2 - \omega^2 + i\gamma_{j\text{TO}}\omega}, \tag{2}$$

where  $\epsilon_\infty$  is the high-frequency dielectric permittivity,  $\omega_{j\text{TO}}$ ,  $\omega_{j\text{LO}}$ ,  $\gamma_{j\text{TO}}$  and  $\gamma_{j\text{LO}}$  correspond to TO and LO

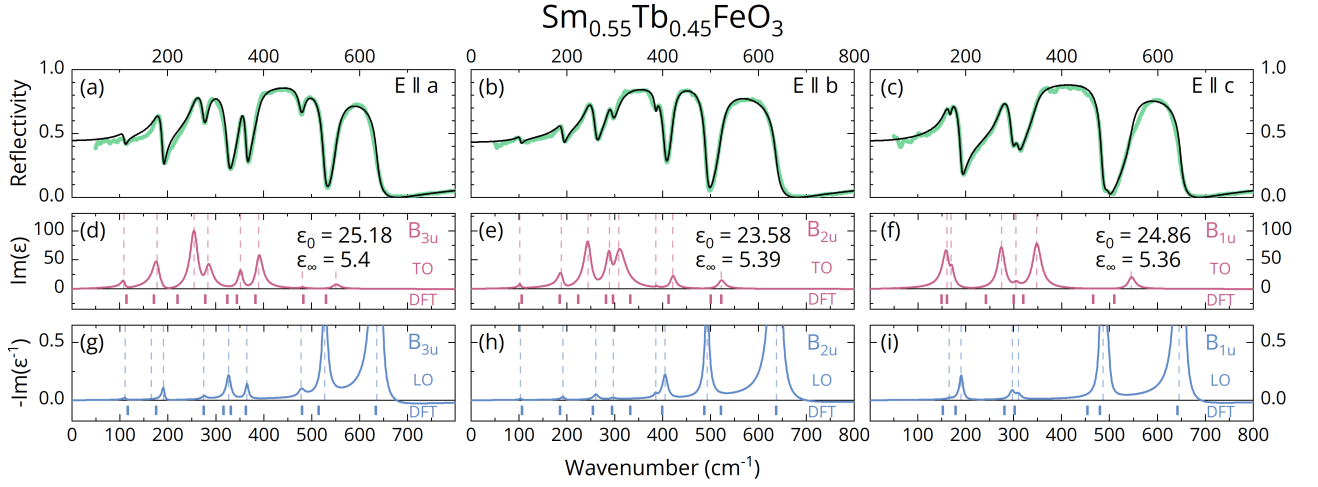


FIG. 2. The infrared reflectivity spectra with the electric field  $\mathbf{E}$  of radiation polarized along the (a)  $a$ , (b)  $b$ , and (c)  $c$  axes of the  $\text{Sm}_{0.55}\text{Tb}_{0.45}\text{FeO}_3$  at room temperature in the  $Pbnm$  setting. The solid black lines are fits using Eq. (3) with a complex dielectric permittivity  $\varepsilon = \varepsilon_1 - i\varepsilon_2$  from Eq. (2). Spectra of the  $\Im[\varepsilon(\omega)]$  and  $-\Im[\varepsilon^{-1}(\omega)]$  from fits which correspond to the TO and LO infrared-active phonons with (d), (g)  $B_{3u}$ , (e), (h)  $B_{2u}$ , and (f), (i)  $B_{1u}$  symmetries, respectively. Vertical dashed gray lines denote the experimental frequencies of infrared-active phonons. Color sticks at the bottom of plots represent the calculated phonon frequencies.

TABLE II. Experimental frequencies  $\omega$  ( $\text{cm}^{-1}$ ), dampings  $\gamma$  ( $\text{cm}^{-1}$ ), and dielectric strengths  $\Delta\varepsilon$  of the TO and LO polar phonons in  $\text{Sm}_{0.55}\text{Tb}_{0.45}\text{FeO}_3$  at room temperature in comparison with the results of DFT calculations presented in parentheses.

Sym.	$\omega_{\text{TO}}$	$\gamma_{\text{TO}}$	$\omega_{\text{LO}}$	$\gamma_{\text{LO}}$	$\Delta\varepsilon$
$B_{1u}$	160.4 (149.4)	18.3	166.9 (152.5)	7.3	7.14 (3.84)
	169.1 (160.8)	9.1	191.2 (179.7)	9.4	1.68 (6.39)
	274.5 (242.5)	18.2	297 (281.4)	11.7	4.74 (9.30)
	304.8 (300.3)	13.8	310 (302.8)	14.3	0.34 (0.52)
	347.8 (320.2)	22	484.8 (454.1)	10.2	4.95 (4.75)
	495.6 (465.8)	14	498 (480.1)	11.1	0.01 (0.11)
	545.5 (510.1)	17.8	647.8 (641.9)	9.8	0.66 (0.60)
$B_{2u}$	102.3 (106.3)	6.9	103.2 (106.5)	6.4	0.45 (0.13)
	188.6 (185.2)	13.3	192.5 (185.7)	9.1	1.56 (0.37)
	244.6 (223.7)	17.9	260.6 (254.5)	12.4	5.77 (14.92)
	289.2 (282.3)	14.2	295.5 (294.6)	11.6	2.87 (7.49)
	308.7 (296.4)	29.1	385.5 (332.7)	6.7	6.29 (1.18)
	386.3 (332.7)	6.7	405.4 (399.1)	13	0.04 (0.00)
	421.5 (412.7)	13.6	492.6 (487)	11	0.69 (0.64)
	— (500.7)	—	— (521.9)	—	— (0.26)
$B_{3u}$	522.5 (522.7)	17.1	636.6 (637)	12	0.49 (0.02)
	109.3 (114.9)	10.2	111 (116.3)	7.8	0.95 (1.04)
	178.7 (171.7)	18.7	190.8 (176)	6.8	4.55 (3.18)
	255.8 (220.9)	19.8	275.3 (274.7)	11.4	7.86 (19.34)
	284.4 (278.8)	18.4	326.9 (316.6)	11.8	2.48 (0.73)
	— (324.9)	—	— (331.5)	—	— (0.27)
	352.1 (344.5)	11.7	365.1 (362.7)	7.9	1.05 (0.91)
	390.2 (383.1)	17.5	478.3 (480.2)	15.2	2.6 (1.79)
	480.9 (483.2)	16.1	527.3 (514.9)	11.8	0.06 (0.05)
	550.7 (530.5)	17.5	636.1 (633.8)	10.2	0.25 (0.20)

frequencies ( $\omega_j$ ) and dampings ( $\gamma_j$ ) of the  $j$ th polar phonon of the specific symmetry, respectively. Multiplication occurs over all polar phonons with the specific symmetry which are active for this polarization of the incident light. We note that Eq. (2) at  $\omega = 0$  converges to the well-known Lyddane-Sachs-Teller relation [49]. For normal incidence, the infrared reflectivity  $R(\omega)$  and complex dielectric function  $\varepsilon(\omega)$  are related to each other via the Fresnel equation [50]

$$R(\omega) = \left| \frac{\sqrt{\varepsilon(\omega)} - 1}{\sqrt{\varepsilon(\omega)} + 1} \right|^2. \quad (3)$$

There is a fair agreement between the reflectivity spectra (green lines) and the fits (black lines) from Eqs. (2) and (3) as can be seen in Figs. 2(a)–2(c). The peaks in the spectra of the imaginary part of the dielectric permittivity  $\Im[\varepsilon(\omega)]$  [Figs. 2(d)–2(f)] and the inverse dielectric permittivity  $\Im[\varepsilon^{-1}(\omega)]$  [Figs. 2(g)–2(i)] correspond to the frequencies of transverse (TO) and longitudinal (LO) polar phonons, respectively [51]. The parameters of the  $B_{1u}$ ,  $B_{2u}$ , and  $B_{3u}$  infrared-active phonons derived from the fits are listed in Table II. The obtained results are close to those reported in the literature for other orthoferrites [45, 52, 53].

The static dielectric permittivity  $\varepsilon_0 = \varepsilon_\infty + \sum_j \Delta\varepsilon_j$  is determined by the infrared-active phonons via their dielectric strengths [54]

$$\Delta\varepsilon_j = \frac{\varepsilon_\infty}{\omega_{j\text{TO}}^2} \frac{\prod_k \omega_{k\text{LO}}^2 - \omega_{j\text{TO}}^2}{\prod_{k \neq j} \omega_{k\text{TO}}^2 - \omega_{j\text{TO}}^2}. \quad (4)$$

The dielectric strengths  $\Delta\varepsilon$  evaluated using Eq. (4) are listed in Table II. The anisotropic static  $\varepsilon_0$  and

high frequency  $\varepsilon_\infty$  dielectric permittivities obtained from fits are given in Figs. 2(a)–2(c). This value of  $\varepsilon_0$  for  $\text{Sm}_{0.55}\text{Tb}_{0.45}\text{FeO}_3$  is in fair agreement with the data reported in the literature on several orthoferrites [8, 52, 55].

### C. Raman-active phonons

The intensity of the light scattered by a Raman-active phonon is determined by the following relation [56]

$$I \propto |\mathbf{e}_s \mathcal{R} \mathbf{e}_i|^2, \quad (5)$$

where  $\mathcal{R}$  is the Raman tensor,  $\mathbf{e}_s$  and  $\mathbf{e}_i$  are the unit vectors of the polarization for the incident and scattered light in the crystal axes coordinate system, respectively. The Raman tensors of Raman-active phonons for  $Pbnm$  orthoferrites are defined as [47, 57]

$$\begin{aligned} \mathcal{R}_{A_g} &= \begin{pmatrix} a_1 & 0 & 0 \\ 0 & a_2 & 0 \\ 0 & 0 & a_3 \end{pmatrix}, & \mathcal{R}_{B_{1g}} &= \begin{pmatrix} 0 & a_4 & 0 \\ a_4 & 0 & 0 \\ 0 & 0 & 0 \end{pmatrix}, \\ \mathcal{R}_{B_{2g}} &= \begin{pmatrix} 0 & 0 & a_5 \\ 0 & 0 & 0 \\ a_5 & 0 & 0 \end{pmatrix}, & \mathcal{R}_{B_{3g}} &= \begin{pmatrix} 0 & 0 & 0 \\ 0 & 0 & a_6 \\ 0 & a_6 & 0 \end{pmatrix}, \end{aligned} \quad (6)$$

where  $a_1$ – $a_6$  are Raman tensor elements. Thus, Raman-active phonons of a given symmetry can be selectively distinguished by using specific polarization configurations of incident and scattered light with respect to the main crystallographic axes of the crystal. The polarization configuration is usually given in Porto's notation, according to which a set of four symbols is used,  $\mathbf{k}_i(\mathbf{e}_i\mathbf{e}_s)\mathbf{k}_s$ , where  $\mathbf{k}_i$  and  $\mathbf{k}_s$  are the directions of the propagation of the incident and scattered light (for the backscattering geometry these directions are opposite  $\mathbf{k}_i = -\mathbf{k}_s$ ) [58]. According to Eqs. (6) and (5), the  $A_g$  phonons are active for the parallel polarization settings  $\mathbf{e}_i \parallel \mathbf{e}_s$  whereas  $B_{1g}$ ,  $B_{2g}$  and  $B_{3g}$  phonons are distinguishable in the crossed configurations  $\mathbf{e}_i \perp \mathbf{e}_s$ .

Figure 3 shows the Raman polarized spectra of  $\text{Sm}_{0.55}\text{Tb}_{0.45}\text{FeO}_3$  at ambient conditions. These spectra were analyzed and  $A_g$ ,  $B_{1g}$ ,  $B_{2g}$ , and  $B_{3g}$  Raman-active phonons were reliably identified in parallel and crossed polarizations, respectively. The small leakage of phonons in forbidden polarizations was observed presumably due to the slight misalignment of the polarization of light with respect to the crystal axes in the samples and the almost unavoidable depolarization effect in the optical elements. The frequencies, full widths at half maximum (FWHMs), and intensities of the Raman-active phonons were extracted by fitting the Raman spectra with a sum of Voigt profiles implemented in FITYK software [59] without Bose correction. These results are listed in Table III. The frequencies of the Raman-active phonons are close to those for other orthoferrites [28–30, 45].

The observed strong asymmetric line with a frequency  $\simeq 630 \text{ cm}^{-1}$  appearing in parallel polarizations only was

TABLE III. Frequencies ( $\text{cm}^{-1}$ ), full widths at half maximum (FWHM,  $\text{cm}^{-1}$ ), and maximal intensity (counts/s) of the Raman-active  $A_g$ ,  $B_{1g}$ ,  $B_{2g}$ , and  $B_{3g}$  phonons for  $\text{Sm}_{0.55}\text{Tb}_{0.45}\text{FeO}_3$  at ambient conditions. The calculated phonon frequencies are given in parentheses.

Sym.	Freq.		FWHM	Intensity
$A_g$	108.7	(111)	2.9	35.4
	139.9	(133.1)	6.1	74.3
	245.5	(245.9)	21.2	31.1
	322.8	(324.1)	9.1	47.9
	392.1	(389.3)	12.6	14.9
	416.7	(405.1)	27.7	9.3
	476.2	(478.9)	13.2	46.9
$B_{1g}$	109.1	(109.9)	3.4	7.5
	156.9	(157)	4.5	49.5
	277.9	(281.4)	20.4	2.9
	—	(349.6)	—	—
	471.2	(473.3)	9.6	9.4
	—	(521.9)	—	—
$B_{2g}$	—	(640.4)	—	—
	132.3	(127.3)	5.6	2.1
	320.8	(314.6)	12.9	1.1
	427.5	(409.9)	18.4	8.5
	459.5	(458)	9.4	3.2
$B_{3g}$	—	(669.1)	—	—
	155.4	(147.5)	5.6	1.6
	241.8	(233)	8.1	3.7
	351.9	(344.6)	5.6	5.8
	424.6	(405.6)	11.9	2.5
	—	(621.9)	—	—

previously reported in  $\text{SmFeO}_3$  [33, 44, 60, 61] and other orthoferrites [44, 60, 62–67]. According to Refs. [44, 67], the frequency and polarization selection rules of this line seem to be independent on the R ions in orthoferrites, including Y. Moreover, the calculated frequencies of the  $A_g$  phonons are lower than this excitation [44, 45, 63]. This allows us to assume that this line is not an  $A_g$  Raman-active phonon, but it is related to the chemical defects in the lattice. However, it is worth noting that intensity and spectra depend on the R ion and this dependence is reproduced for different orthoferrite crystals of the same composition. While this line exhibits low intensity in  $\text{TbFeO}_3$  [30, 44, 45], its intensity is markedly greater in  $\text{SmFeO}_3$  [44] and in  $\text{Sm}_{0.55}\text{Tb}_{0.45}\text{FeO}_3$ .

### D. Magnons

There are four  $\text{Fe}^{3+}$  ions in the orthoferrite unit cell, which gives two doubly degenerate magnon branches called acoustic and exchange. The Dzyaloshinskii-Moriya interaction leads to a net magnetic moment due to a small spin canting ( $\simeq 8.5 \text{ mrad}$ ) and splitting of the magnon branches [1]. The acoustic branch is split on the quasi-ferromagnetic (qFM,  $\simeq 10 \text{ cm}^{-1}$ ) and quasi-



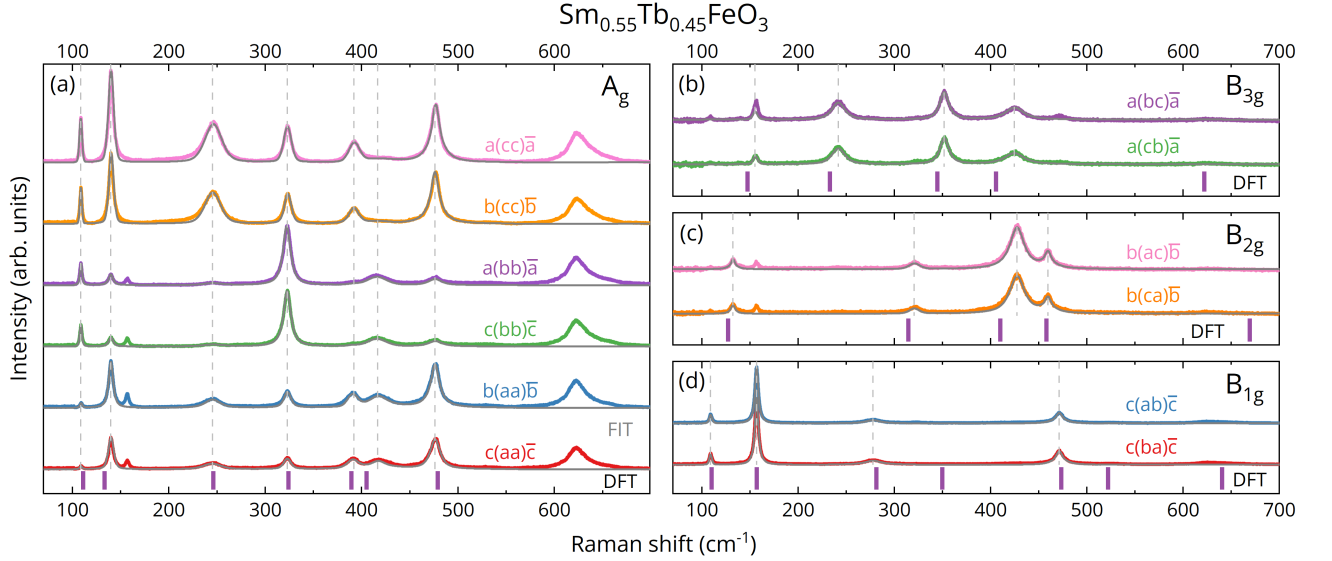


FIG. 3. The polarized Raman scattering spectra of the (a)  $A_g$ , (b)  $B_{3g}$ , (c)  $B_{2g}$ , and (d)  $B_{1g}$  phonons for  $\text{Sm}_{0.55}\text{Tb}_{0.45}\text{FeO}_3$  at ambient conditions. The polarization configurations are given in Porto's notation as described in the text in the  $Pbnm$  setting. The solid gray lines are fits of the phonons active in the corresponding polarization configuration as described in the text. The frequencies of these phonons are denoted by the vertical dashed lines. Purple sticks at the bottom of each plot represent the calculated phonon frequencies.

antiferromagnetic (qAFM,  $\simeq 20 \text{ cm}^{-1}$ ) magnon modes. These modes can be represented as the precession of the ferromagnetic vector  $\mathbf{M} = \mathbf{M}_A + \mathbf{M}_B$  for qFM [see Fig. 1(c)], and antiferromagnetic vector  $\mathbf{L} = \mathbf{M}_A - \mathbf{M}_B$  for qAFM [see Fig. 1(d)] magnon modes, where  $\mathbf{M}_A$  and  $\mathbf{M}_B$  are magnetizations of the oppositely directed sublattices. The exchange magnon branch ( $\simeq 450 \text{ cm}^{-1}$ ) is also split by the Dzyaloshinskii-Moriya interaction, but it interacts extremely weakly with light, but appears in inelastic neutron scattering experiments [27]. However, the splitting of acoustic and exchange magnon branches cannot be resolved in neutron experiments.

The qFM and qAFM magnon modes in orthoferrites are clearly visible in Raman scattering [28, 30, 62, 68], pump-probe [17, 69] and THz [1, 8, 9, 52, 55] experiments. The Raman tensors for qFM and qAFM magnon modes for orthoferrites in the  $Pbnm$  setting are given for low-temperature  $\Gamma_2$  magnetic structure [70]

$$\begin{aligned} \mathcal{R}_{\text{qFM}}^{\Gamma_2}(B_g) &= \begin{pmatrix} 0 & b_1 & b_2 \\ b_3 & 0 & 0 \\ b_4 & 0 & 0 \end{pmatrix}, \\ \mathcal{R}_{\text{qAFM}}^{\Gamma_2}(A_g) &= \begin{pmatrix} b_5 & 0 & 0 \\ 0 & b_6 & b_7 \\ 0 & b_8 & b_9 \end{pmatrix}, \end{aligned} \quad (7)$$

and for high-temperature  $\Gamma_4$  magnetic structure [28, 70,

71]

$$\begin{aligned} \mathcal{R}_{\text{qFM}}^{\Gamma_4}(B_g) &= \begin{pmatrix} 0 & 0 & c_1 \\ 0 & 0 & c_2 \\ c_3 & c_4 & 0 \end{pmatrix}, \\ \mathcal{R}_{\text{qAFM}}^{\Gamma_4}(A_g) &= \begin{pmatrix} c_5 & c_6 & 0 \\ c_7 & c_8 & 0 \\ 0 & 0 & c_9 \end{pmatrix}, \end{aligned} \quad (8)$$

where  $b_1$ – $b_9$  and  $c_1$ – $c_9$  are Raman tensor elements.

The Raman scattering spectra in the range from  $-20$  to  $20 \text{ cm}^{-1}$  for all parallel and crossed polarization configurations along main crystal axes for the  $\Gamma_2$  at  $T = 78 \text{ K}$  (left panels with blue shaded area) and  $\Gamma_4$  at  $293 \text{ K}$  (right panels with red shaded area) magnetic structures in  $\text{Sm}_{0.55}\text{Tb}_{0.45}\text{FeO}_3$  are shown in Fig. 4. It is clearly seen anti-Stokes and Stokes lines of the two excitations with frequencies  $\simeq \pm 7 \text{ cm}^{-1}$  and  $\simeq \pm 18 \text{ cm}^{-1}$  in the high-temperature  $\Gamma_4$  phase and only one line at  $\simeq \pm 7$  in the low-temperature  $\Gamma_2$  magnetic structure. The highest Raman scattering intensities for the  $\simeq \pm 7 \text{ cm}^{-1}$  mode are observed in the  $a(bc)\bar{a}$  [ $a(cb)\bar{a}$ ] for the  $\Gamma_4$  and in the  $c(ab)\bar{c}$  [ $c(ba)\bar{c}$ ] polarization configurations for the  $\Gamma_2$  magnetic structure. The excitation with a frequency  $\simeq \pm 18 \text{ cm}^{-1}$  clearly seen in the  $\Gamma_4$  magnetic structure has the highest Raman scattering intensity in the  $c(ab)\bar{c}$  [ $c(ba)\bar{c}$ ] polarization configuration, while we could not reliably detect it in the  $\Gamma_2$  phase. Therefore, the selection rules from the Raman tensors (7) and (8) and typical values of frequencies allow us to assign these excitations to qFM ( $\simeq \pm 7 \text{ cm}^{-1}$ ) and qAFM ( $\simeq \pm 18 \text{ cm}^{-1}$ ) magnon modes.

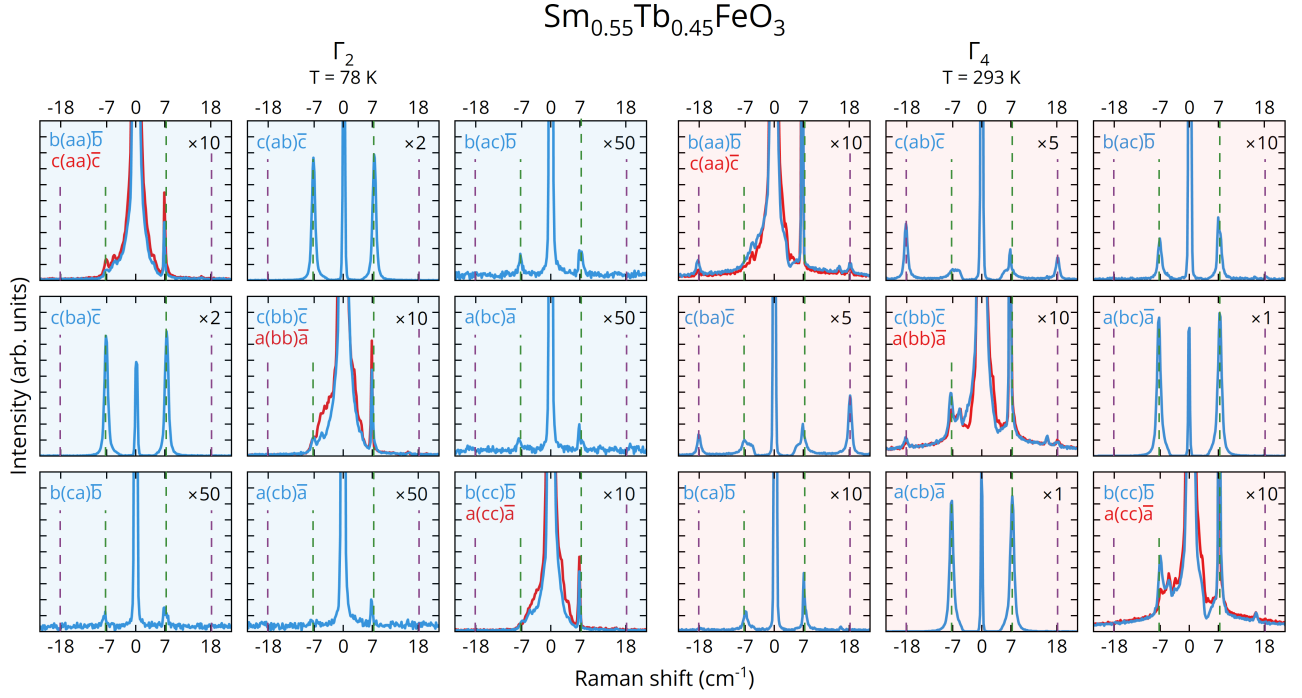


FIG. 4. The polarized Raman scattering spectra of the quasi-ferromagnetic (qFM,  $\simeq \pm 7 \text{ cm}^{-1}$ ) and quasi-antiferromagnetic (qAFM,  $\simeq \pm 18 \text{ cm}^{-1}$ ) modes in  $\text{Sm}_{0.55}\text{Tb}_{0.45}\text{FeO}_3$  in  $\Gamma_2$  (blue shaded area,  $T = 78 \text{ K}$ ) and  $\Gamma_4$  (red shaded area,  $T = 293 \text{ K}$ ) magnetic structures. The polarization configurations are given in Porto's notation as described in the text in the  $Pbnm$  setting. The intensity of some spectra is multiplied by a factor denoted by the “ $\times$ ” sign to highlight the weaker excitations.

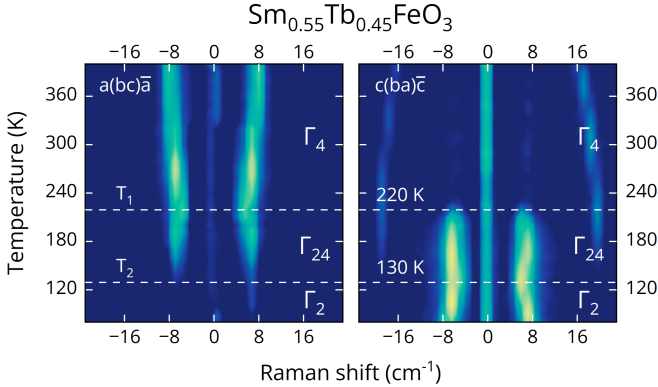


FIG. 5. The temperature color map of the polarized Raman scattering spectra of quasi-ferromagnetic (qFM,  $\simeq \pm 7 \text{ cm}^{-1}$ ) and quasi-antiferromagnetic (qAFM,  $\simeq \pm 18 \text{ cm}^{-1}$ ) modes in  $\text{Sm}_{0.55}\text{Tb}_{0.45}\text{FeO}_3$  in the  $a(bc)\bar{a}$  (left panel) and  $c(ba)\bar{c}$  (right panel) polarization configurations which are given in Porto's notation as described in the text in the  $Pbnm$  setting. The  $\Gamma_4$ ,  $\Gamma_{24}$  and  $\Gamma_2$  magnetic structures separated by the white dashed lines. The intensity is given on a log scale.

### E. Spin reorientation transition

Next, we measured the temperature dependence of the Raman scattering spectra from 400 to 78 K in the  $a(cb)\bar{a}$  and  $c(ba)\bar{c}$  polarization configurations. It is clearly seen that in the  $a(bc)\bar{a}$  polarization configuration (left panel

in Fig. 5) the qFM magnon mode is active at temperatures above  $\simeq 130 \text{ K}$ , whereas above and below  $\simeq 130 \text{ K}$  we could not observe any evidence of the qAFM magnon mode. On the contrary, in the  $c(ba)\bar{c}$  polarization configuration (right panel in Fig. 5) the qAFM magnon mode has been detected at temperatures above  $\simeq 130 \text{ K}$ , and below  $\simeq 220 \text{ K}$  the qFM mode becomes active. This allows us to conclude that the spin reorientation transitions  $\Gamma_4(G_a F_c) \xleftrightarrow{T_1} \Gamma_{24}(G_{ac} F_{ac}) \xleftrightarrow{T_2} \Gamma_2(G_a F_c)$  with  $T_1 \simeq 220 \text{ K}$  and  $T_2 \simeq 130 \text{ K}$  is realized in the  $\text{Sm}_{0.55}\text{Tb}_{0.45}\text{FeO}_3$ .

We note that according to the literature, the Raman scattering from the qAFM magnon mode has not been detected in the  $\Gamma_2$  magnetic structure in other orthoferites, e.g. in  $\text{ErFeO}_3$  [28, 29, 68],  $\text{SmFeO}_3$  [68],  $\text{TmFeO}_3$  and  $\text{TbFeO}_3$  [30, 62]. However, the qAFM magnon mode is clearly seen in the  $\Gamma_2$  magnetic structure in the magnetodipole absorption [9]. On the other hand, for the  $\Gamma_1$  magnetic structure, which is present at low temperatures in  $\text{DyFeO}_3$ , the qAFM magnon mode has been revealed in the Raman scattering [68] and the THz experiments [8, 72].

To better understand the temperature behavior of magnetic excitations across spin reorientation transitions, we fit the Raman scattering spectra from Fig. 5 using the procedure described earlier. The results are shown in Figs. 6(a)–6(g). The frequency of the qFM magnon mode shows a soft mode behavior and has two minima at temperatures  $T_1 \simeq 220 \text{ K}$  and  $T_2 \simeq 130 \text{ K}$

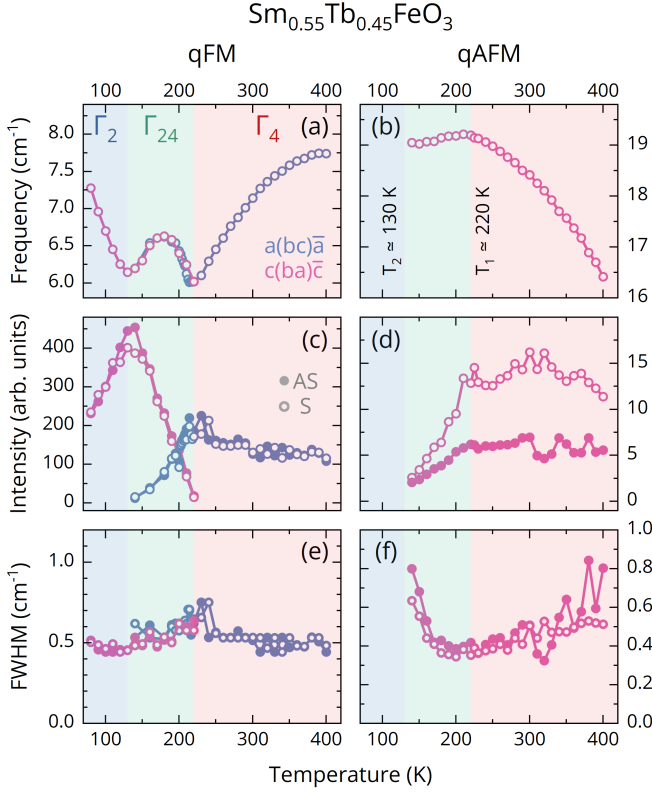


FIG. 6. The temperature dependences of (a, b) frequency, (c, d) intensity and (e, f) full widths at half maximum (FWHM) of the anti-Stokes (AS, closed circles) and Stokes (S, open circles) Raman scattering lines in the  $a(bc)\bar{a}$  and  $c(ba)\bar{c}$  polarization configurations of the qFM and qAFM magnon excitations, respectively. The blue, green, and red shaded areas correspond to the  $\Gamma_2$  ( $T < 130$  K),  $\Gamma_{24}$  ( $130$  K  $< T < 220$  K), and  $\Gamma_4$  ( $T > 220$  K) magnetic configurations, respectively. Intensities were not Bose corrected.

as can be seen in Fig. 6(a). Moreover, the  $\omega_{\text{qFM}}$  at  $T_1$  and  $T_2$  has non-zero values, which is related to a magnetoelastic gap in the magnon spectrum ( $\simeq 6$  cm $^{-1}$ ) due to the magnetoelastic interaction of the quasi-ferromagnetic mode with acoustic phonon [73]. This soft mode behavior of the qFM magnon mode frequency was previously observed in Raman scattering on other orthoferrites with the  $\Gamma_4(G_a F_c) \xleftrightarrow{T_1} \Gamma_{24}(G_{ac} F_{ac}) \xleftrightarrow{T_2} \Gamma_2(G_c F_a)$  transition, e.g. in  $\text{ErFeO}_3$  [29],  $\text{TmFeO}_3$  [30, 62]. At that, the qAFM mode is not a soft mode and its frequency increases at cooling in the  $\Gamma_4$  magnetic structure and remains almost constant after the transition to the  $\Gamma_{24}$  magnetic structure, as shown for the  $c(ba)\bar{c}$  polarization configuration in Fig. 6(b).

It should be emphasized that the temperature range  $\Delta T = T_1 - T_2 \simeq 90$  K in which the intermediate magnetic structure  $\Gamma_{24}$  is realized is unusually wide in  $\text{Sm}_{0.55}\text{Tb}_{0.45}\text{FeO}_3$  compared to other rare-earth orthoferrites with  $\Gamma_4(G_a F_c) \xleftrightarrow{T_1} \Gamma_{24}(G_{ac} F_{ac}) \xleftrightarrow{T_2} \Gamma_2(G_c F_a)$  transitions [14], as can be seen for some crystals in Table IV. Next, we will try to understand what causes such a wide

TABLE IV. Temperatures  $T_1$  and  $T_2$  (in K) of the spin reorientation transitions  $\Gamma_4 \xleftrightarrow{T_1} \Gamma_{24} \xleftrightarrow{T_2} \Gamma_2$  and temperature ranges  $\Delta T = T_1 - T_2$  in which the intermediate magnetic structure  $\Gamma_{24}$  is realized for the earth-rare orthoferrites.

	$T_1$	$T_2$	$\Delta T = T_1 - T_2$
$\text{TbFeO}_3^{\text{a}}$	9	8	1
$\text{TmFeO}_3^{\text{b}}$	94	84	10
$\text{ErFeO}_3^{\text{c}}$	103	90	13
$\text{Sm}_{0.7}\text{Er}_{0.3}\text{FeO}_3^{\text{d}}$	330	310	20
$\text{NdFeO}_3^{\text{e}}$	170	107	63
$\text{PrFeO}_3^{\text{e}}$	10	6.5	3.5
$\text{Sm}_{0.4}\text{Er}_{0.6}\text{FeO}_3^{\text{f}}$	210	175	35
$\text{Sm}_{0.7}\text{Tb}_{0.3}\text{FeO}_3^{\text{g}}$	330	310	20
$\text{SmFeO}_3^{\text{h}}$	360	330	30
$\text{Sm}_{0.55}\text{Tb}_{0.45}\text{FeO}_3^{\text{i}}$	220	130	90
$\text{Sm}_{0.5}\text{Tb}_{0.5}\text{FeO}_3^{\text{j}}$	250	150	100

<sup>a</sup> Refs. [9, 55, 74, 75].

<sup>b</sup> Ref. [30].

<sup>c</sup> Ref. [68].

<sup>d</sup> Ref. [76].

<sup>e</sup> Ref. [77].

<sup>f</sup> Ref. [78].

<sup>g</sup> Ref. [35].

<sup>h</sup> Ref. [32].

<sup>i</sup> This work.

<sup>j</sup> Ref. [26].

temperature range  $\Delta T$  in  $\text{Sm}_{0.55}\text{Tb}_{0.45}\text{FeO}_3$ . The frequencies of magnon modes in orthoferrites are described by the following expressions [79]

$$\omega_{\text{qFM}} = \frac{\gamma}{m_0} \sqrt{H_{\text{ex}} H_{ac}}, \quad \omega_{\text{qAFM}} = \frac{\gamma}{m_0} \sqrt{H_{\text{ex}} H_{ab}}, \quad (9)$$

where  $\gamma$  is the gyromagnetic ratio,  $m_0$  is the magnetization of the  $\text{Fe}^{3+}$  sublattices, and  $H_{\text{ex}}$  is the exchange field. According to Ref. [79], the effective anisotropy field  $H_{ac}$  and  $H_{ab}$  have the form

$$H_{ac}(T) = \begin{cases} K_{ac}^{\text{eff}}(T), & T > T_1, \\ 2 \sqrt{-\frac{K_{ac}^{\text{eff}}(T)}{K_2} \left[ 1 + \frac{K_{ac}^{\text{eff}}(T)}{K_2} \right]}, & T_2 < T < T_1, \\ K_{ca}^{\text{eff}}(T) = -2K_2 - K_{ac}^{\text{eff}}(T), & T_2 > T, \end{cases} \quad (10)$$

and

$$H_{ab}(T) = \begin{cases} K_{ab}^0, & T > T_1, \\ K_{ab}^0 + \left[ 1 + \frac{K_{ac}^{\text{eff}}(T)}{K_2} \right] (K_2'' + K_2), & T_2 < T < T_1, \\ K_{ab}^0 + K_2'' + K_2, & T_2 > T, \end{cases} \quad (11)$$

which includes the anisotropy function

$$K_{ac}^{\text{eff}}(T) = K_{ac}^0 - \frac{(\Delta_{\text{ex}}^0)^2}{(\tilde{T} - \tilde{\lambda}_f)^2} (2\tilde{T} - \tilde{\lambda}_f), \quad (12)$$

$$K_{ca}^{\text{eff}}(T) = -2K_2 - K_{ac}^{\text{eff}}(T),$$



and crystallographic anisotropy constants  $K_{ac}^0$ ,  $K_{ab}^0$ ,  $K_2$ ,  $K_2''$ . Here,  $\Delta_{ex}^0$  is the exchange parameter,  $\Delta_{cf}$  is the crystal field splitting,  $\Delta_R(T) = \sqrt{\Delta_{ex}^2(T) + \Delta_{cf}^2}$  is the energy splitting parameter,  $\tilde{T} = \Delta_R / \tanh(\Delta_R/T)$  is the reduced temperature, and  $\tilde{\lambda}_f$  is the parameter, which represents  $f$ - $f$  exchange interaction.

The temperature dependence of the magnon mode frequencies  $\omega_{qFM}(T)$  and  $\omega_{qAFM}(T)$  in  $\text{Sm}_{0.55}\text{Tb}_{0.45}\text{FeO}_3$  can be fairly described using the parameters  $K_{ac}^0 = 0.326$  K,  $K_2 = 0.128$  K,  $\Delta_{cf} = 67$  K, and  $\Delta_{ex}^0 = 5.55$  K. These parameters lie within the range predicted by theory, as detailed in Ref. [80], and are in good agreement with the Refs. [79, 81, 82], where similar parameters for other orthoferrites have been reported. Since here we deal with the orthoferrite with the mixed rare-earth dopants, these parameters are understood as “effective” and mostly refer to the  $\text{Sm}^{3+}$  ions, for which  $\Delta_{cf}$  is much larger than for  $\text{Tb}^{3+}$ .

To understand further the origin of the spin reorientation transition temperature range (i.e. interval between  $T_1$  and  $T_2$ ), let us assume a high-temperature approximation valid for  $T_{1,2} \gg 10$  K, so that the parameters responsible for the low-temperature  $f$ - $f$  exchange can be neglected. The spin reorientation transition is caused by the zero crossing of the effective anisotropy functions at temperatures  $T_1$  and  $T_2$ . Then Eq. (12) for the effective anisotropies at the phase transition temperatures from Ref. [79] will take the following form:

$$\begin{aligned} K_{ac}^{\text{eff}}(T_1) &= K_{ac} - 2(\Delta_{ex}^0)^2 \frac{\tanh(\Delta_{cf}/T_1)}{\Delta_{cf}} = 0, \\ K_{ca}^{\text{eff}}(T_2) &= -2K_{ac} - K_{ac} + 2(\Delta_{ex}^0)^2 \frac{\tanh(\Delta_{cf}/T_1)}{\Delta_{cf}} = 0 \end{aligned} \quad (13)$$

By solving them with respect to  $T_1$  and  $T_2$ , one can obtain the following solutions:

$$\begin{aligned} T_1 &= \frac{\Delta_{cf}}{\text{arctanh}\left[\frac{K_{ac}^0 \Delta_{cf}}{2(\Delta_{ex}^0)^2}\right]}, \\ T_2 &= \frac{\Delta_{cf}}{\text{arctanh}\left[\frac{(2K_2 + K_{ac}^0) \Delta_{cf}}{2(\Delta_{ex}^0)^2}\right]}. \end{aligned} \quad (14)$$

It turns out to be convenient to analyze the ratio between  $T_1$  and  $T_2$  which has the following form:

$$\frac{T_1}{T_2} = \frac{\text{arctanh}\left[\frac{K_{ac}^0 \Delta_{cf}}{2(\Delta_{ex}^0)^2}\right]}{\text{arctanh}\left[\frac{(2K_2 + K_{ac}^0) \Delta_{cf}}{2(\Delta_{ex}^0)^2}\right]}. \quad (15)$$

From this ratio, it can be seen that by setting cubic anisotropy  $K_2$  to zero, the ratio will be equal to 1, corresponding to the scenario with only one second-order phase transition occurring at  $T_1$ . In the course of  $\Gamma_4 \xrightarrow{T_1} \Gamma_{24} \xrightarrow{T_2} \Gamma_2$  spin reorientation transitions, which

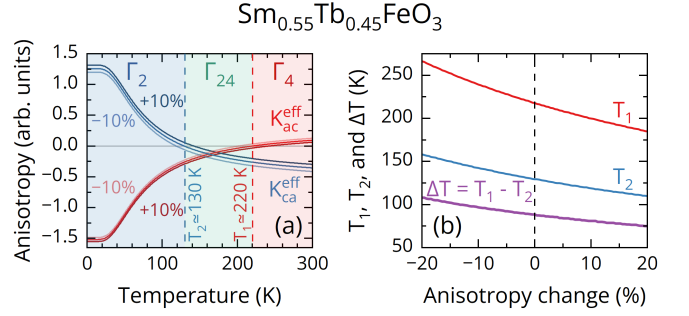


FIG. 7. (a) The temperature dependences over the spin reorientation transitions interval for the effective anisotropy functions  $K_{ca}^{\text{eff}}(T)$  and  $K_{ac}^{\text{eff}}(T)$  which determine the temperatures of the transitions  $\Gamma_4 \xrightarrow{T_1} \Gamma_{24} \xrightarrow{T_2} \Gamma_2$ . The change  $\pm 10\%$  in the anisotropies leads to a change in  $T_1 \simeq 193 - 232$  K and  $T_2 \simeq 121 - 145$  K. (b) Temperatures of spin reorientation transitions  $T_1$  and  $T_2$  and temperature ranges  $\Delta T = T_1 - T_2$  of the intermediate magnetic structure  $\Gamma_{24}$  as functions of the magnetic anisotropy.

manifest themselves as two second-order phase transitions, at  $T_1$  and  $T_2$  and is observed in most of the orthoferrites, the value of  $K_2$  must be positive [83]. For our parameters, the value of this ratio is  $\Delta T \simeq 0.4967$ . By varying parameters included in Eq. (15) individually by  $\pm 10\%$  while keeping the others constant, we obtain that for  $K_{ac} = 0.358$  K, the ratio changes to  $\Delta T \simeq 0.509$ ; for  $K_2 = 0.1408$  K it becomes  $\Delta T \simeq 0.467$ ; for  $\Delta_{cf} = 73.6$  K we evaluated a value  $\Delta T \simeq 0.479$ ; and for  $\Delta_{ex}^0 = 6.1$  K it has taken on a value  $\Delta T \simeq 0.519$ . Thus, the change in the anisotropy constant  $K_2$  has a stronger effect on the spin reorientation transition temperature range  $\Delta T$  than corresponding changes in  $K_{ac}$ ,  $\Delta_{cf}$  and  $\Delta_{ex}^0$ , even though they are all of the same order. Therefore, it can be concluded that the existence of the spin reorientation transition is primarily defined by the cubic anisotropy  $K_2$ . The temperature interval is mostly determined by the balancing of values of the cubic anisotropy  $K_2$  and crystallographic anisotropy  $K_{ac}$  as well as their ratio to the crystal field  $\Delta_{cf}$  and exchange interaction parameter  $\Delta_{ex}^0$ . The doping of  $\text{SmFeO}_3$  with  $\text{Tb}^{3+}$  ions dilutes the concentration of Sm ions and introduces defects into the magnetic texture, which in turn modifies the values of effective anisotropy parameters.

Figure 7(a) shows the temperature dependences of the effective anisotropies  $K_{ca}^{\text{eff}}(T)$  and  $K_{ac}^{\text{eff}}(T)$  according to Eq. (12) when only anisotropy parameters  $K_2$  and  $K_{ac}^0$  are varied by  $\pm 10\%$ . The crossing of the zero by  $K_{ac}^{\text{eff}}(T)$  and  $K_{ca}^{\text{eff}}(T)$  occurs at the transition temperatures  $T_1$  and  $T_2$ . It can be seen that a decrease in anisotropies leads to a lowering in these temperatures. Moreover, the temperature  $T_1$  changes with a change in anisotropy more strongly than  $T_2$ , which in turn leads to an increase in the temperature range  $\Delta T$ , as shown in Fig. 7(b). Thus, in the mixed sample the value of the effective anisotropy is different from the pure orthoferrites due to the random distribution of the  $\text{Sm}^{3+}$  and  $\text{Tb}^{3+}$  ions, making

the magnetic structure defected, which may explain the broad temperature interval of the spin reorientation.

The intensities for the anti-Stokes and Stokes lines of the qFM mode have close temperature behavior as can be seen in Fig. 6(c). It depends weakly on the temperature for  $a(bc)\bar{a}$  polarization configuration in the  $\Gamma_4$  magnetic structure, and at the transition to the intermediate  $\Gamma_{24}$  magnetic structure, the intensity begins to decrease sharply to extremely low values at cooling. In the  $c(ab)\bar{c}$  the intensity of the qFM mode begins to rapidly increase at cooling in the  $\Gamma_{24}$  magnetic structure, but at the transition in the  $\Gamma_2$  magnetic structure, the trend changes and it gradually decreases. At that, the FWHM of the qFM mode is about  $0.5\text{ cm}^{-1}$  and weakly dependent on the temperature for both polarization configurations [see Fig. 6(e)].

As already stated, the qAFM mode does not appear in any polarization configurations in the  $\Gamma_2$  magnetic structure. It is clearly seen in Fig. 4, the intensity of the Stokes Raman line is greater than the anti-Stokes one of the qAFM mode in the  $c(ba)\bar{c}$  polarization configuration in the  $\Gamma_4$  magnetic structure. These intensities are essentially unchanged in the  $\Gamma_4$  magnetic structure, whereas in the  $\Gamma_{24}$  magnetic structure at cooling they sharply decrease to almost very low values as shown in Fig. 6(d). The FWHM decreases at cooling and does not change significantly at  $\Gamma_4(G_a, F_c) \xleftrightarrow{T_1} \Gamma_{24}(G_{ac}, F_{ac})$  magnetic transition after which it rises, which is probably due to the difficulty of determining the FWHM of lines with low intensities.

Since the temperature dependences of the Raman scattering of magnetic excitations were measured in the range from  $-180$  to  $180\text{ cm}^{-1}$ , this allowed us to trace the behavior of two  $B_{1g}$  phonons ( $\simeq 110\text{ cm}^{-1}$  and  $\simeq 157\text{ cm}^{-1}$ ) which are active in the  $c(ab)\bar{c}$  polarization configuration [see Figs. 3(d), 8(a) and Table III]. The Stokes lines in Raman scattering spectra of these phonons were fitted using the procedure described earlier which allowed us to derive the temperature dependences of the frequency, intensity and FWHM as shown in Fig. 8(b)–8(g), respectively. All of them have a typical behavior for Raman-active phonons, with the frequency increasing and the intensity and FWHM decreasing. Moreover, it is clearly seen that the parameters of these  $B_{1g}$  Raman-active phonons do not show any noticeable change at the temperatures  $T_1 \simeq 220\text{ K}$  and  $T_2 \simeq 130\text{ K}$  which allows us to conclude that this phonon is not susceptible to the  $\Gamma_4(G_a, F_c) \xleftrightarrow{T_1} \Gamma_{24}(G_{ac}, F_{ac}) \xleftrightarrow{T_2} \Gamma_2(G_a, F_c)$  spin reorientation transitions. This conclusion is further supported by the fact that the involvement of Fe ions in Raman-active phonons is forbidden by symmetry [45]. The absence of any evidences of spin-phonon coupling for Raman-active phonons at the antiferromagnetic ordering of Fe ions below  $T_N$  has been observed previously in rare-earth orthoferrites [32]. Moreover, the lattice parameters of orthoferrites also show no clear change at  $T_N$  [84]. However, it was reported in Ref. [33] that slight

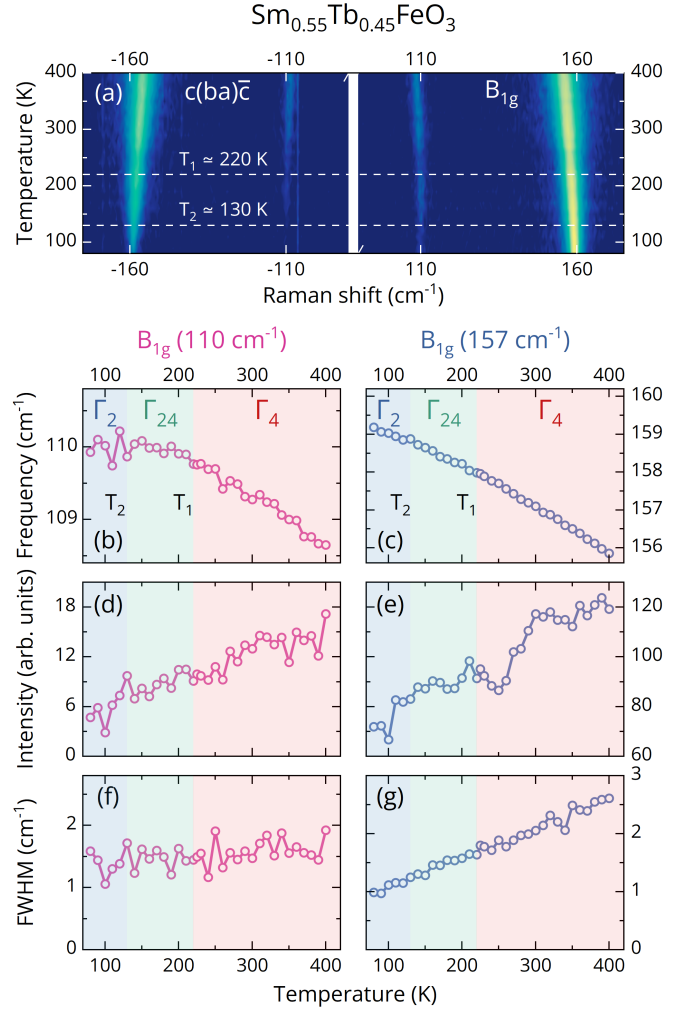


FIG. 8. (a) The temperature color map of the polarized Raman spectra for the  $c(ab)\bar{c}$  polarization configuration in the range that involves low-frequency  $B_{1g}$  phonons. The intensity is given on a log scale. The temperature dependences of (b, c) frequency, (d, e) intensity and (f, g) full widths at half maximum (FWHM) of the Stokes Raman scattering lines of the two low-frequency  $B_{1g}$  phonon from panel (a). The blue, green, and red shaded areas correspond to the  $\Gamma_2$  ( $T < 130\text{ K}$ ),  $\Gamma_{24}$  ( $130\text{ K} < T < 220\text{ K}$ ), and  $\Gamma_4$  ( $T > 220\text{ K}$ ) magnetic configurations, respectively. Intensities were not Bose corrected.

changes in the frequency of some Raman-active phonons at the spin-spin reorientation transitions were detected in polycrystalline  $\text{SmFeO}_3$  samples.

It is known that rare earth ions are significantly involved in the vibration of the lowest frequency Raman-active phonon in orthoferrites [45]. The magnetism of iron induces a non-spontaneous polarization of the rare earth ion spins which is manifested in the shift of phonon frequencies and the appearance of new phonon lines as a result of possible symmetry lowering [1, 32]. A further important result of our experimental study is the absence of any evidence of new  $B_{1g}$  phonon lines in the temperature color map in Fig. 8(a) and no apparent devi-

ation of parameters of the lowest frequency  $B_{1g}$  phonons from anharmonic behavior, as can be seen in Figs. 8(b)–8(g). This strongly indicates that the rare earth ions in  $\text{Sm}_{0.55}\text{Tb}_{0.45}\text{FeO}_3$  do not experience non-spontaneous polarization under the action of the iron sublattice at the specified temperature range.

#### IV. CONCLUDING REMARKS

In summary, we have scrutinized the lattice and magnetic dynamics at the center of the Brillouin zone of the rare-earth orthoferrite  $\text{Sm}_{0.55}\text{Tb}_{0.45}\text{FeO}_3$  single crystal by the polarized spectroscopic infrared and Raman scattering technique. The obtained experimental results on the lattice dynamics were supported by the first-principles calculations, which allowed us to reliably identify the parameters of most infrared- and Raman-active phonons. Further, we explored the Raman scattering spectra of the quasi-ferromagnetic mode and quasi-antiferromagnetic mode in all main polarization configurations at temperatures 78 K and 293 K which correspond to the  $\Gamma_2$  and  $\Gamma_4$  magnetic structures in this compound, respectively.

Then, we studied the temperature dependence from 78 K to 400 K of the spectra in which the Raman scattering of the quasi-ferromagnetic and quasi-antiferromagnetic modes is most intense in the  $\Gamma_2$  and  $\Gamma_4$  magnetic structures. As a result, it was found that a sequence of spin reorientation transitions  $\Gamma_4 \xleftrightarrow{T_1} \Gamma_{24} \xleftrightarrow{T_2} \Gamma_2$  is observed at the temperatures  $T_1 \simeq 220$  K and  $T_2 \simeq 130$  K in the  $\text{Sm}_{0.55}\text{Tb}_{0.45}\text{FeO}_3$ . At that, the quasi-ferromagnetic mode is a soft mode the frequency of which does not go to zero due to magnetoelastic interaction. The theoretical analysis demonstrates that the temperature range of the intermediate magnetic phase  $\Gamma_{24}$  is primarily controlled by the magnetocrystalline anisotropy. The random distribution of rare-earth  $\text{Sm}^{3+}$  and  $\text{Tm}^{3+}$  ions introduces defects into the magnetic lattice of  $\text{Sm}_{0.55}\text{Tb}_{0.45}\text{FeO}_3$  compared to pure orthoferrites. This alters to a change in the magnetocrystalline anisotropy, resulting in an increased temperature range

$\Delta T = T_1 - T_2 \simeq 90$  K for the  $\Gamma_{24}$  phase. We have not found any clear evidence for Raman scattering of the quasi-antiferromagnetic mode in the  $\Gamma_2$  magnetic structure. Furthermore, we have revealed that the two lowest frequency  $B_{1g}$  Raman-active phonons do not show any obvious changes at both spin-reorientation transitions, which we attribute to the fact that the involvement of the Fe ions in the Raman-active phonons is forbidden by symmetry. We believe that our findings will stimulate further experimental research into the booming field of nonlinear phononic, magnetophononic and spin-related effects in the rare-earth orthoferrites [17, 18, 21–25, 85].

#### ACKNOWLEDGEMENTS

We thank N.A. Arkhipov for the help with the XRD orientation and Dr. G.A. Gusev and Prof. M.V. Zamoryanskaya for the XRF characterization of single crystals, G.V. Osochenko for assistance in experimental research. This work was supported by the Russian Science Foundation under Grant No. 24-72-00106, <https://rscf.ru/en/project/24-72-00106/>. A.I.B. acknowledges the support of the Ministry of Science and Higher Education of the Russian Federation (Grant No. FSWR-2024-0003). V.A.C. also acknowledges the support of the Ministry of Science and Higher Education of the Russian Federation (Grant No. FEUZ-2023-0017). N.N.N. acknowledges the support of the research project FFUU-2025-0004 of the Institute of Spectroscopy of the Russian Academy of Sciences. A.W. and L.S. acknowledge the support of the National Natural Science Foundation of China (NSFC, Nos. 52272014, W2421113), and the International Partnership Program of Chinese Academy of Sciences (No. 030GJHZ2024093MI). R.V.M. acknowledges the support of Royal Society International Exchanges 2021, grant IES\R2\212182.

#### DATA AVAILABILITY

The data that support the findings of this article are openly available [86].

- 
- [1] X. Li, D. Kim, Y. Liu, and J. Kono, Terahertz spin dynamics in rare-earth orthoferrites, *Photonics Insights* **1**, R05 (2023).
  - [2] A. Sasani, J. Íñiguez, and E. Bousquet, Origin of nonlinear magnetoelectric response in rare-earth orthoferrite perovskite oxides, *Phys. Rev. B* **105**, 064414 (2022).
  - [3] E. Bousquet and A. Cano, Non-collinear magnetism in multiferroic perovskites, *J. Phys.: Condens. Matter* **28**, 123001 (2016).
  - [4] Y. Tokunaga, S. Iguchi, T. Arima, and Y. Tokura, Magnetic-Field-Induced Ferroelectric State in  $\text{DyFeO}_3$ , *Phys. Rev. Lett.* **101**, 097205 (2008).
  - [5] V. Y. Ivanov, A. M. Kuzmenko, A. Y. Tikhanovskii, and A. A. Mukhin, Metamagnetic and orientational transitions in  $\text{TbFeO}_3$  orthoferrite: magnetoelectric phase diagrams, *Eur. Phys. J. Plus* **138**, 1 (2023).
  - [6] V. Y. Ivanov, A. M. Kuzmenko, A. Y. Tikhanovskii, A. A. Pronin, and A. A. Mukhin, Observation of Magnetic-Field-Induced Electric Polarization in Terbium Orthoferrite, *JEPT Lett.* **117**, 38–43 (2023).
  - [7] A. P. Pyatakov and A. K. Zvezdin, Magnetoelectric and multiferroic media, *Phys.-Usp.* **55**, 557 (2012).
  - [8] T. N. Stanislavchuk, Y. Wang, Y. Janssen, G. L. Carr, S.-W. Cheong, and A. A. Sirenko, Magnon and electromagnon excitations in multiferroic  $\text{DyFeO}_3$ , *Phys. Rev.*

TABLE V. Calculated frequencies ( $\text{cm}^{-1}$ ) of the phonons at the Brillouin zone center in rare-earth orthoferrites  $\text{TbFeO}_3$ ,  $\text{SmFeO}_3$ , and  $\text{Sm}_{0.55}\text{Tb}_{0.45}\text{FeO}_3$ . The procedure for estimating the phonon frequencies for  $\text{Sm}_{0.55}\text{Tb}_{0.45}\text{FeO}_3$  using those for  $\text{TbFeO}_3$  and  $\text{SmFeO}_3$  is described in detail in the main text.

Sym.	$\text{TbFeO}_3$	$\text{SmFeO}_3$	$\text{Sm}_{0.55}\text{Tb}_{0.45}\text{FeO}_3$	Sym.	$\text{TbFeO}_3$		$\text{SmFeO}_3$		$\text{Sm}_{0.55}\text{Tb}_{0.45}\text{FeO}_3$	
					TO	LO	TO	LO	TO	LO
$A_g$	111.8	110.3	111	$B_{1u}$	146.3	152	151.9	152.9	149.4	152.5
	131.8	134.2	133.1		158.1	177.6	163.1	181.4	160.8	179.7
	253.1	240	245.9		241.3	283	243	280	242.2	281.4
	330	319.3	324.1		302.6	303.7	298.4	302.1	300.3	302.8
	402.4	378.6	389.3		326.2	455.1	315.3	453.3	320.2	454.1
	408.8	402	405.1		467.3	482.1	464.6	478.5	465.8	480.1
	487.6	471.7	478.9		511	643.2	509.4	640.9	510.1	641.9
$B_{1g}$	109.6	110.2	109.9	$B_{2u}$	104.4	104.7	107.8	108	106.3	106.5
	157.8	156.4	157		185.9	186.7	184.6	184.8	185.2	185.7
	293.9	271.2	281.4		224.5	256.3	223	253	223.7	254.5
	351.7	347.9	349.6		288.8	295.6	277	293.7	282.3	294.6
	483.1	465.3	473.3		297.7	336.7	295.3	329.5	296.4	332.7
	529.3	515.8	521.9		336.7	401.4	329.5	397.3	332.7	399.1
	641.1	639.8	640.4		417.2	494.5	409	480.8	412.7	487
$B_{2g}$	122.6	131.1	127.3	$B_{3u}$	506.6	527.3	495.9	517.5	500.7	521.9
	314.3	314.8	314.6		528.5	642.7	517.9	632.3	522.7	637
	412.4	407.8	409.9		114.7	116.1	115.1	116.4	114.9	116.3
	463.7	453.4	458		171.5	176	171.8	176	171.7	176
	667.8	670.2	669.1		221.8	275.9	220.1	273.8	220.9	274.7
$B_{3g}$	140.9	152.9	147.5		280.7	318.7	277.2	314.8	278.8	316.6
	239.8	227.4	233		328.4	334	322.1	329.4	324.9	331.5
	347.8	342	344.6		347.3	369.4	342.2	357.2	344.5	362.7
	409.6	402.3	405.6		392.2	492	375.6	470.6	383.1	480.2
	622.8	621.1	621.9		495.7	519.9	473	510.9	483.2	514.9
$A_u$	79	84.5	82		535.4	638.7	526.5	629.7	530.5	633.8
	155.6	158.2	157		308		307.5		307.7	
	182.9	182.5	182.7		343.2		330.7		336.3	
	220.5	225.4	223.2		456.8		456.3		456.5	
					503.6		495.5		499.1	

- B **93**, 094403 (2016).
- [9] T. N. Stanislavchuk, Y. Wang, S.-W. Cheong, and A. A. Sirenko, Far-IR magnetospectroscopy of magnons and electromagnons in  $\text{TbFeO}_3$  single crystals at low temperatures, *Phys. Rev. B* **95**, 054427 (2017).
- [10] L. Šmejkal, J. Sinova, and T. Jungwirth, Emerging Research Landscape of Altermagnetism, *Phys. Rev. X* **12**, 040501 (2022).
- [11] A. V. Kimel, T. Rasing, and B. A. Ivanov, Optical read-out and control of antiferromagnetic néel vector in altermagnets and beyond, *J. Magn. Magn. Mater.* **598**, 172039 (2024).
- [12] M. Naka, Y. Motome, and H. Seo, Altermagnetic perovskites, *npj Spintronics* **3**, 1 (2025).
- [13] C. Song, H. Bai, Z. Zhou, L. Han, H. Reichlova, J. H. Dil, J. Liu, X. Chen, and F. Pan, Altermagnets as a new class of functional materials, *Nat. Rev. Mater.*, 1 (2025).
- [14] Q. Li, J. Zhou, J. Shang, H. Shen, L. Li, F. Wang, H. Wang, X. Shen, T. Tian, A. Kalashnikova, A. M. Kalashnikova, A. Wu, and J. Xu, Recent advances of rare earth orthoferrite  $\text{RFeO}_3$  magneto-optical single crystals, *J. Cryst. Growth* **649**, 127939 (2025).
- [15] A. V. Kimel, A. Kirilyuk, A. Tsvetkov, R. V. Pisarev, and T. Rasing, Laser-induced ultrafast spin reorientation in the antiferromagnet  $\text{TmFeO}_3$ , *Nature* **429**, 850 (2004).
- [16] A. V. Kimel, B. A. Ivanov, R. V. Pisarev, P. A. Usachev, A. Kirilyuk, and T. Rasing, Inertia-driven spin switching in antiferromagnets, *Nature Phys.* **5**, 727 (2009).
- [17] T. T. Gareev, A. Sasani, D. I. Khusyainov, E. Bousquet, Z. V. Gareeva, A. V. Kimel, and D. Afanasiev, Optical Excitation of Coherent THz Dynamics of the Rare-Earth Lattice through Resonant Pumping of  $f$ - $f$  Electronic Transition in a Complex Perovskite  $\text{DyFeO}_3$ , *Phys. Rev. Lett.* **133**, 246901 (2024).
- [18] R. A. Leenders, D. Afanasiev, A. V. Kimel, and R. V. Mikhaylovskiy, Canted spin order as a platform for ultrafast conversion of magnons, *Nature* **630**, 335–339 (2024).
- [19] D. M. Juraschek, M. Fechner, and N. A. Spaldin, Ultrafast Structure Switching through Nonlinear Phononics, *Phys. Rev. Lett.* **118**, 054101 (2017).
- [20] S. Baierl, M. Hohenleutner, T. Kampfrath, A. K. Zvezdin, A. V. Kimel, R. Huber, and R. V. Mikhaylovskiy, Nonlinear spin control by terahertz-driven anisotropy fields, *Nat. Photon.* **10**, 715 (2016).



- [21] Z. Zhang, F. Y. Gao, Y.-C. Chien, Z.-J. Liu, J. B. Curtis, E. R. Sung, X. Ma, W. Ren, S. Cao, P. Narang, A. von Hoegen, E. Baldini, and K. A. Nelson, Terahertz-field-driven magnon upconversion in an antiferromagnet, *Nat. Phys.* **20**, 788 (2024).
- [22] Z. Zhang, F. Y. Gao, J. B. Curtis, Z.-J. Liu, Y.-C. Chien, A. von Hoegen, M. T. Wong, T. Kurihara, T. Suemoto, P. Narang, E. Baldini, and K. A. Nelson, Terahertz field-induced nonlinear coupling of two magnon modes in an antiferromagnet, *Nat. Phys.* **20**, 801 (2024).
- [23] Z. Zhang, M. Kanega, K. Maruyama, T. Kurihara, M. Nakajima, T. Tachizaki, M. Sato, Y. Kanemitsu, and H. Hirori, Spin switching in  $\text{Sm}_{0.7}\text{Er}_{0.3}\text{FeO}_3$  triggered by terahertz magnetic-field pulses, *Nat. Mater.* **24**, 219 (2025).
- [24] T. F. Nova, A. Cartella, A. Cantaluppi, M. Först, D. Bossini, R. V. Mikhaylovskiy, A. V. Kimel, R. Merlin, and A. Cavalleri, An effective magnetic field from optically driven phonons, *Nature Phys.* **13**, 132 (2017).
- [25] D. Afanasiev, J. R. Hortensius, B. A. Ivanov, A. Sasani, E. Bousquet, Y. M. Blanter, R. V. Mikhaylovskiy, A. V. Kimel, and A. D. Caviglia, Ultrafast control of magnetic interactions via light-driven phonons, *Nat. Mater.* **20**, 607 (2021).
- [26] X. Zhao, K. Zhang, X. Liu, B. Wang, K. Xu, S. Cao, A. Wu, L. Su, and G. Ma, Spin reorientation transition in  $\text{Sm}_{0.5}\text{Tb}_{0.5}\text{FeO}_3$  orthoferrite single crystal, *AIP Adv.* **6**, 10.1063/1.4939697 (2016).
- [27] S. M. Shapiro, J. D. Axe, and J. P. Remeika, Neutron-scattering studies of spin waves in rare-earth orthoferrites, *Phys. Rev. B* **10**, 2014 (1974).
- [28] R. M. White, R. J. Nemanich, and C. Herring, Light scattering from magnetic excitations in orthoferrites, *Phys. Rev. B* **25**, 1822 (1982).
- [29] N. Koshizuka and S. Ushioda, Inelastic-light-scattering study of magnon softening in  $\text{ErFeO}_3$ , *Phys. Rev. B* **22**, 5394 (1980).
- [30] S. Venugopalan, M. Dutta, A. K. Ramdas, and J. P. Remeika, Magnetic and vibrational excitations in rare-earth orthoferrites: A Raman scattering study, *Phys. Rev. B* **31**, 1490 (1985).
- [31] H. Wang, Q. Li, L. Su, H. Kou, A. M. Kalashnikova, and A. Wu, Continuous two spin reorientation transitions and spin flips along the b-axis in  $\text{Er}_{0.6}\text{Gd}_{0.4}\text{FeO}_3$  single crystal, *Phys. B Condens. Matter* **705**, 417109 (2025).
- [32] M. C. Weber, M. Guennou, D. M. Evans, C. Toulouse, A. Simonov, Y. Kholina, X. Ma, W. Ren, S. Cao, M. A. Carpenter, B. Dkhil, M. Fiebig, and J. Kreisel, Emerging spin-phonon coupling through cross-talk of two magnetic sublattices, *Nat. Commun.* **13**, 1 (2022).
- [33] A. Panchwatee, A. Surampalli, and V. R. Reddy, Temperature dependent dielectric and phonon study of polycrystalline  $\text{SmFeO}_3$ , *Phys. B: Condens. Matter* **570**, 187 (2019).
- [34] A. Wu, B. Wang, X. Zhao, T. Xie, P. Man, L. Su, A. M. Kalashnikova, and R. V. Pisarev, Crystal growth of  $\text{Sm}_{0.3}\text{Tb}_{0.7}\text{FeO}_3$  and spin reorientation transition in  $\text{Sm}_{1-x}\text{Tb}_x\text{FeO}_3$  orthoferrite, *J. Magn. Magn. Mater.* **426**, 721 (2017).
- [35] B. Wang, X. Zhao, A. Wu, S. Cao, J. Xu, A. M. Kalashnikova, and R. V. Pisarev, Single crystal growth and magnetic properties of  $\text{Sm}_{0.7}\text{Tb}_{0.3}\text{FeO}_3$  orthoferrite single crystal, *J. Magn. Magn. Mater.* **379**, 192 (2015).
- [36] A. D. Becke, Density-functional thermochemistry. III. The role of exact exchange, *J. Chem. Phys.* **98**, 5648 (1993).
- [37] R. Dovesi, R. Orlando, A. Erba, C. M. Zicovich-Wilson, B. Civalieri, S. Casassa, L. Maschio, M. Ferrabone, M. De La Pierre, P. d'Arco, *et al.*, CRYSTAL14: A program for the *ab initio* investigation of crystalline solids, *Int. J. Quantum Chem.* **114**, 1287 (2014).
- [38] M. Dolg, H. Stoll, A. Savin, and H. Preuss, Energy-adjusted pseudopotentials for the rare earth elements, *Theor. Chim. Acta* **75**, 173 (1989).
- [39] M. Dolg, H. Stoll, and H. Preuss, A combination of quasirelativistic pseudopotential and ligand field calculations for lanthanoid compounds, *Theor. Chim. Acta* **85**, 441 (1993).
- [40] J. Yang and M. Dolg, Valence basis sets for lanthanide 4f-in-core pseudopotentials adapted for crystal orbital ab initio calculations, *Theor. Chem. Acc.* **113**, 212 (2005).
- [41] M. F. Peintinger, D. V. Oliveira, and T. Bredow, Consistent gaussian basis sets of triple-zeta valence with polarization quality for solid-state calculations, *J. Comp. Chem.* **34**, 451 (2013).
- [42] L. Maschio, B. Kirtman, R. Orlando, and M. Rérat, Ab initio analytical infrared intensities for periodic systems through a coupled perturbed Hartree-Fock/Kohn-Sham method, *J. Chem. Phys.* **137**, 204113 (2012).
- [43] L. Maschio, B. Kirtman, M. Rérat, R. Orlando, and R. Dovesi, Ab initio analytical Raman intensities for periodic systems through a coupled perturbed Hartree-Fock/Kohn-Sham method in an atomic orbital basis. I. Theory, *J. Chem. Phys.* **139**, 164101 (2013).
- [44] M. C. Weber, M. Guennou, H. J. Zhao, J. Iñiguez, R. Vilarinho, A. Almeida, J. A. Moreira, and J. Kreisel, Raman spectroscopy of rare-earth orthoferrites  $R\text{FeO}_3$  ( $r = \text{La, Sm, Eu, Gd, Tb, Dy}$ ), *Phys. Rev. B* **94**, 214103 (2016).
- [45] R. M. Dubrovin, E. M. Roginskii, V. A. Chernyshev, N. N. Novikova, M. A. Elistratova, I. A. Elisseyev, A. N. Smirnov, A. I. Brulev, K. N. Boldyrev, V. Y. Davydov, R. V. Mikhaylovskiy, A. M. Kalashnikova, and R. V. Pisarev, Lattice dynamics and mixing of polar phonons in the rare-earth orthoferrite  $\text{TbFeO}_3$ , *Phys. Rev. B* **110**, 134310 (2024).
- [46] T. Yamaguchi, Theory of spin reorientation in rare-earth orthochromites and orthoferrites, *J. Phys. Chem. Solids* **35**, 479 (1974).
- [47] E. Kroumova, M. I. Aroyo, J. M. Perez-Mato, A. Kirov, C. Capillas, S. Ivantchev, and H. Wondratschek, Bilbao crystallographic server: useful databases and tools for phase-transition studies, *Phase Transit.* **76**, 155 (2003).
- [48] F. Gervais and B. Piriou, Anharmonicity in several-polar-mode crystals: adjusting phonon self-energy of LO and TO modes in  $\text{Al}_2\text{O}_3$  and  $\text{TiO}_2$  to fit infrared reflectivity, *J. Phys. C: Solid State Phys.* **7**, 2374 (1974).
- [49] R. H. Lyddane, R. G. Sachs, and E. Teller, On the Polar Vibrations of Alkali Halides, *Phys. Rev.* **59**, 673 (1941).
- [50] M. Born and E. Wolf, *Principles of Optics: Electromagnetic Theory of Propagation, Interference and Diffraction of Light* (Elsevier, 2013).
- [51] M. Schubert, *Infrared Ellipsometry on Semiconductor Layer Structures: Phonons, Plasmons, and Polaritons*, Vol. 209 (Springer Science & Business Media, 2004).



- [52] G. A. Komandin, A. M. Kuzmenko, I. E. Spektor, and A. A. Mukhin, Electric-dipole and magnetic absorption in TbFeO<sub>3</sub> single crystals in the THz–IR range, *J. Appl. Phys.* **133**, 194101 (2023).
- [53] M. M. Gomes, R. Vilarinho, H. Zhao, J. Íñiguez González, M. Mihalik, M. Mihalik, A. Maia, V. Goian, D. Nuzhnyy, S. Kamba, and J. A. Moreira, Lattice excitations in NdFeO<sub>3</sub> through polarized optical spectroscopies, *Sci. Rep.* **14**, 15378 (2024).
- [54] F. Gervais and H. Arend, Long-wavelength phonons in the four phases of {N(CH<sub>3</sub>)<sub>4</sub>}<sub>2</sub>CuCl<sub>4</sub> and effective charges, *Z. Phys. B* **50**, 17 (1983).
- [55] A. M. Balbashov, G. V. Kozlov, A. A. Mukhin, and A. S. Prokhorov, High frequency processes in magnetic materials (World Scientific Publishing, Singapore, 1995) Chap. Submillimeter spectroscopy of antiferromagnetic dielectrics. Rare-earth orthoferrites.
- [56] R. Loudon, The Raman effect in crystals, *Adv. Phys.* **50**, 813 (2001).
- [57] L. Martín-Carrón and A. De Andrés, Melting of the cooperative Jahn-Teller distortion in LaMnO<sub>3</sub> single crystal studied by Raman spectroscopy, *Eur. Phys. J. B* **22**, 11 (2001).
- [58] T. C. Damen, S. P. S. Porto, and B. Tell, Raman Effect in Zinc Oxide, *Phys. Rev.* **142**, 570 (1966).
- [59] M. Wojdyr, Fityk: a general-purpose peak fitting program, *J. Appl. Crystallogr.* **43**, 1126 (2010).
- [60] S. Gupta, R. Medwal, S. P. Pavunny, D. Sanchez, and R. S. Katiyar, Temperature dependent raman scattering and electronic transitions in rare earth SmFeO<sub>3</sub>, *Ceram. Int.* **44**, 4198 (2018).
- [61] M. K. Warshi, A. Kumar, A. Sati, S. Thota, K. Mukherjee, A. Sagdeo, and P. R. Sagdeo, Cluster glass behavior in orthorhombic SmFeO<sub>3</sub> perovskite: Interplay between spin ordering and lattice dynamics, *Chem. Mater.* **32**, 1250 (2020).
- [62] S. Venugopalan, M. Dutta, A. K. Ramdas, and J. P. Re-meika, Raman scattering study of magnons at the spin-reorientation transitions of TbFeO<sub>3</sub> and TmFeO<sub>3</sub>, *Phys. Rev. B* **27**, 3115 (1983).
- [63] H. C. Gupta, M. Kumar Singh, and L. M. Tiwari, Lattice dynamic investigation of Raman and infrared wavenumbers at the zone center of orthorhombic RFeO<sub>3</sub> (R = Tb, Dy, Ho, Er, Tm) perovskites, *J. Raman Spectrosc.* **33**, 67 (2002).
- [64] P. V. Coutinho, F. Cunha, and P. Barrozo, Structural, vibrational and magnetic properties of the orthoferrites LaFeO<sub>3</sub> and YFeO<sub>3</sub>: A comparative study, *Solid State Commun.* **252**, 59 (2017).
- [65] S. Raut, P. D. Babu, R. K. Sharma, R. Pattanayak, and S. Panigrahi, Grain boundary-dominated electrical conduction and anomalous optical-phonon behaviour near the neel temperature in YFeO<sub>3</sub> ceramics, *J. Appl. Phys.* **123**, 10.1063/1.5012003 (2018).
- [66] B. S. Nagrare, S. S. Kekade, B. Thombare, R. V. Reddy, and S. I. Patil, Hyperfine interaction, Raman and magnetic study of YFeO<sub>3</sub> nanocrystals, *Solid State Commun.* **280**, 32 (2018).
- [67] Y. S. Ponosov and D. Y. Novoselov, Lattice and spin excitations of YFeO<sub>3</sub>: A Raman and density functional theory study, *Phys. Rev. B* **102**, 054418 (2020).
- [68] N. Koshizuka and K. Hayashi, Raman Scattering from Magnon Excitations in RFeO<sub>3</sub>, *J. Phys. Soc. Japan* **57**, 4418 (1988).
- [69] A. V. Kimel, A. Kirilyuk, P. A. Usachev, R. V. Pisarev, A. M. Balbashov, and T. Rasing, Ultrafast non-thermal control of magnetization by instantaneous photomagnetic pulses, *Nature* **435**, 655 (2005).
- [70] V. Bar'yakhtar, Y. G. Pashkevich, and V. Sobolev, Light scattering by magnons and magneto-optical effects in multisublattice magnets, *Zh. Eksp. Teor. Fiz.* **85**, 1625 (1983).
- [71] A. P. Cracknell, Scattering matrices for the Raman effect in magnetic crystals, *J. Phys. C Solid State Phys.* **2**, 500 (1969).
- [72] A. M. Balbashov, A. A. Volkov, S. P. Lebedev, A. A. Mukhin, and A. S. Prokhorov, High-frequency magnetic properties of dysprosium orthoferrite, *Zh. Eksp. Teor. Fiz* **88**, 974 (1985).
- [73] E. A. Turov and V. G. Shavrov, Broken symmetry and magnetoacoustic effects in ferro and antiferromagnetics, *Sov. Phys. Usp.* **26**, 593 (1983).
- [74] O. Nikolov, I. Hall, S. N. Barilo, and S. A. Guretskii, A Mossbauer study of temperature-driven spin-reorientation transitions in TbFeO<sub>3</sub>, *J. Phys. Condens. Matter* **6**, 3793 (1994).
- [75] S. Artyukhin, M. Mostovoy, N. P. Jensen, D. Le, K. Prokes, V. G. De Paula, H. N. Bordallo, A. Maljuk, S. Landsgesell, H. Ryll, B. Klemke, S. Paegel, K. Kiefer, K. Lefmann, L. T. Kuhn, and D. N. Argyriou, Solitonic lattice and Yukawa forces in the rare-earth orthoferrite TbFeO<sub>3</sub>, *Nat. Mater.* **11**, 694 (2012).
- [76] G. Fitzky, M. Nakajima, Y. Koike, A. Leitenstorfer, and T. Kurihara, Ultrafast Control of Magnetic Anisotropy by Resonant Excitation of 4f Electrons and Phonons in Sm<sub>0.7</sub>Er<sub>0.3</sub>FeO<sub>3</sub>, *Phys. Rev. Lett.* **127**, 107401 (2021).
- [77] E. Li, Z. Feng, B. Kang, J. Zhang, W. Ren, and S. Cao, Spin switching in single crystal PrFeO<sub>3</sub> and spin configuration diagram of rare earth orthoferrites, *Journal of Alloys and Compounds* **811**, 152043 (2019).
- [78] A. Wu, X. Zhao, P. Man, L. Su, A. M. Kalashnikova, and R. V. Pisarev, Growth, and magnetic study of Sm<sub>0.4</sub>Er<sub>0.6</sub>FeO<sub>3</sub> single crystal grown by optical floating zone technique, *J. Cryst. Growth* **486**, 169 (2018).
- [79] N. R. Vovk, E. V. Ezerskaya, and R. V. Mikhaylovskiy, Theory of terahertz-driven magnetic switching in rare-earth orthoferrites: The case of TmFeO<sub>3</sub>, *Phys. Rev. B* **111**, 064411 (2025).
- [80] A. K. Zvezdin, V. M. Matveev, A. A. Mukhin, and A. I. Popov, *Rare earth ions in magnetically ordered crystals* (1985).
- [81] V. D. Buchel'nikov, N. K. Dan'shin, L. Tsymbal, and V. G. Shavrov, Magnetoacoustics of rare-earth orthoferrites, *Phys.-Usp.* **39**, 547 (1996).
- [82] A. M. Balbashov, G. V. Kozlov, S. P. Lebedev, A. A. Mukhin, A. Y. Pronin, and A. S. Prokhorov, Anomalies of high-frequency magnetic properties and new orientational transitions in HoFeO<sub>3</sub>, *Sov. Phys. JETP* **68**, 629 (1989).
- [83] K. P. Belov, A. K. Zvezdin, A. M. Kadomtseva, and R. Z. Levitin, Spin-reorientation transitions in rare-earth magnets, *Sov. Phys. Uspekhi* **19**, 574 (1976).
- [84] O. Pavlovskaya, L. Vasylechko, and O. Buryy, Thermal behaviour of Sm<sub>0.5</sub>R<sub>0.5</sub>FeO<sub>3</sub> (R = Pr, Nd) probed by high-resolution X-ray synchrotron powder diffraction, *Nanoscale Res. Lett.* **11**, 1 (2016).

- [85] C. Huang, L. Luo, M. Mootz, J. Shang, P. Man, L. Su, I. E. Perakis, Y. X. Yao, A. Wu, and J. Wang, Extreme terahertz magnon multiplication induced by resonant magnetic pulse pairs, [Nat. Commun. \*\*15\*\*, 3214 \(2024\)](#).
- [86] R. M. Dubrovin, A. I. Brulev, N. R. Vovk, I. A. Eliseyev, N. N. Novikova, A. N. Smirnov, V. A. Chernyshev, V. Y. Davydov, A. Wu, L. Su, R. V. Mikhaylovskiy, A. M. Kalashnikova, and R. V. Pisarev, Dataset for spin and lattice dynamics at the spin-reorientation transitions in the rare-earth orthoferrite  $\text{Sm}_{0.55}\text{Tb}_{0.45}\text{FeO}_3$ , [10.5281/zenodo.XXXXXXXX](#) (2025).